

# On the Size and Spacing of Volcanogenic Massive Sulfide Deposits within a District with Application to the Matagami District, Quebec

PATRICK M. CARR,<sup>†,\*</sup> LAWRENCE M. CATHLES III,

*Department of Earth and Atmospheric Sciences, 2122 Snee Hall, Cornell University, Ithaca, New York 14850*

AND C. TUCKER BARRIE

*C.T. Barrie and Associates, 29 Euclid Avenue, Ottawa, Ontario, Canada K1S 2W2*

## Abstract

Volcanogenic massive sulfide (VMS) districts are typically ~40 km in diameter and contain about a dozen regularly spaced Zn-Cu orebodies, one or two of which contain more than half of the district's resources. We numerically investigate this deposit size and spatial distribution by calculating zinc transport across the sea floor, first above sills of simple geometry, and then above the Bell River Complex at Matagami. For sills with simple rectangular geometry (i.e., a constant thickness), convection is strongest at the edge. The edge convection induces a progression of convection cells above the sill, although the sill cools mainly by the retreat of its thermal edges toward the sill center. If the rock permeability is a function of temperature that is maximized at 375°C, the resulting vents occur at stable, discrete locations that proxy for ore deposits. The fraction of sill heat vented at or above 300°C and the potential metal resources of the districts are greatest if the host permeability is 10<sup>-15</sup> m<sup>2</sup> (1 millidarcy) and the sill top is at 1 km depth. The simulations suggest that, as the host permeability increases, a single large deposit will progressively dominate a host of smaller ones. The Matagami simulations are based on a sill that tapers from 6.5 to 0 km thickness over a distance of 30 km. In the model, convection occurs both above the sill and along its underside, and metal is extracted from both sides of the cooling sill. The spacing of the resulting discharge sites is similar to that observed in actual VMS districts and, where direct comparison is possible, the mass of metal deposited is similar for an accumulation efficiency of ~3 percent.

## Introduction

VMS DEPOSITS form where seawater, heated to ~350°C by subsurface igneous intrusions, discharges into the ocean and is thermally and chemically quenched. Sulfides accumulating near zinc- and iron-rich black smoker vents at midocean ridges provide a present-day analogue (Kelley et al., 2002). Typically, a dozen or so VMS deposits form in ~40-km-diameter areas of bimodal volcanism. One or two very large deposits often contain half of the total ore metal in these districts, and a third of the deposits generally contain a very high percentage of the total ore. For example, the Matagami Lake deposit contains 40 percent of the zinc resource in the Matagami district; 42 percent of the deposits contain 96 percent of the zinc resource (internal data of Xstrata Zinc). The Home deposit contains 44 percent of the zinc resource in the Noranda district; 34 percent of the deposits contain 85 percent of the zinc resource (Gibson and Watkinson, 1990). Matsumine contains 26 percent of the zinc resources in the Hokuroku district of Japan; 34 percent of the deposits contain 85 percent of the zinc resources (Tanimura et al., 1983). To our knowledge, this fundamental size distribution has never been explicitly addressed by modeling. Here we investigate its possible origins through numerical simulation of the convective cooling of sill intrusions.

Many numerical models of the convective cooling of intrusions have been published. Lapwood (1948), and more recently Trubitsyn et al. (1993) and Rosenberg et al. (1993)

modeled convection above an infinite horizontal hot plate which can be thought of as a sill with no edge. In these circumstances, convection occurs only if a dimensionless combination of parameters (e.g., depth of convection, permeability, heat input) called the Rayleigh number exceeds a critical value. Cheng and Minkowycz (1977), Parmentier (1979), and Cheng and Pop (1984) modeled the single convection cell that develops adjacent to a hot vertical surface. Here, no critical Rayleigh number need be exceeded, because the vertical edge of the intrusion imposes horizontal temperature and fluid density gradients in the adjacent rock, and these force convection. Cathles (1977), Norton and Knight (1977), and Cathles (1983) modeled the convective cooling of a tabular pluton with exposed vertical edges that was narrow enough that only a single hydrothermal plume formed above the intrusion. A wider intrusion produces separate discharges above each edge with inflow over the intrusion top (Cathles, 1978). Multiple upwellings also occur above a broad sill-like intrusion (Brikowski and Norton, 1989; Schardt et al., 2005). Barrie et al. (1999) and Erendi (2000) have explicitly modeled convection by sill-shaped intrusions as we shall here.

These models provide a useful background but have not systematically investigated the number and size of deposits that might form over sills emplaced at varying depths into hosts of varying permeability. These are the objectives of this paper.

## Model Construction for Heuristic Cases

The simulations we report here are based on finite element solutions to the porous media conservation equations of mass, momentum, and energy. The equations, solution methods,

<sup>†</sup> Corresponding author: e-mail, pmc1@cornell.edu

\* Present address: Xstrata Zinc Canada, 500, boulevard Industriel, Matagami, Québec, Canada J0Y 2A0.

boundary and initial conditions, parameters, and convergence criteria used are described in the Appendix. We deliberately keep our simulations as simple as possible so that the effects of intrusion geometry, depth of emplacement, and host permeability can be isolated. Rock permeability is taken to be constant, modified only as a function of temperature at temperatures greater than 275°C (to simulate thermal cracking and render the hottest portions of the sill impermeable, as discussed below). Thermal conductivity is constant, but is augmented by thermal dispersion, which is significant where convection is rapid. Media heat capacity is constant; the latent heat of crystallization of the magma is not included. Fluid heat capacity and viscosity are constant (not dependent on temperature and pressure), and fluid density varies linearly with temperature. Variations in water properties in the supercritical region are not included, and fluid boiling is not simulated. These phenomena could be important, and we discuss their possible contributions in the final section of this paper.

The two-dimensional computational domain used in all simple sill computations is shown in Figure 1. The domain is 10 km wide and 10 km deep and is divided into quadrants of common rectilinear grid refinement. The upper left quadrant

(above and including the sill) is the most refined; this allows resolution of convection in the steep temperature gradients that form at the edge of the sill. For sills deeper than shown in Figure 1, the refinement is adjusted to keep the element sizes unchanged.

The boundary conditions used in the calculations are shown in Figure 1 and defined mathematically in the Appendix. A heat flux of 42 mW/m<sup>2</sup> is imposed at the base. The top boundary is set at 2°C unless the advective heat flux across the sea floor exceeds 2 mW/m<sup>2</sup>, in which case the thermal gradient normal to the boundary is set to zero and the pore waters are allowed to vent into the ocean with no change in temperature as they cross the surface. The boundary condition is switched only in elements of water outflow. The simulation results are not sensitive to the magnitude of the heat flux that triggers the boundary condition change, so we adopt a low heat flux trigger. Free fluid flow is allowed across the top boundary, and no flow is allowed through the sides or bottom.

The initial temperature distribution is set in two steps. First, the temperature is set at the steady-state distribution for a basal heat flow of 42 mW/m<sup>2</sup>. For the constant thermal conductivity of 2 W/m/°C, temperature increases from the

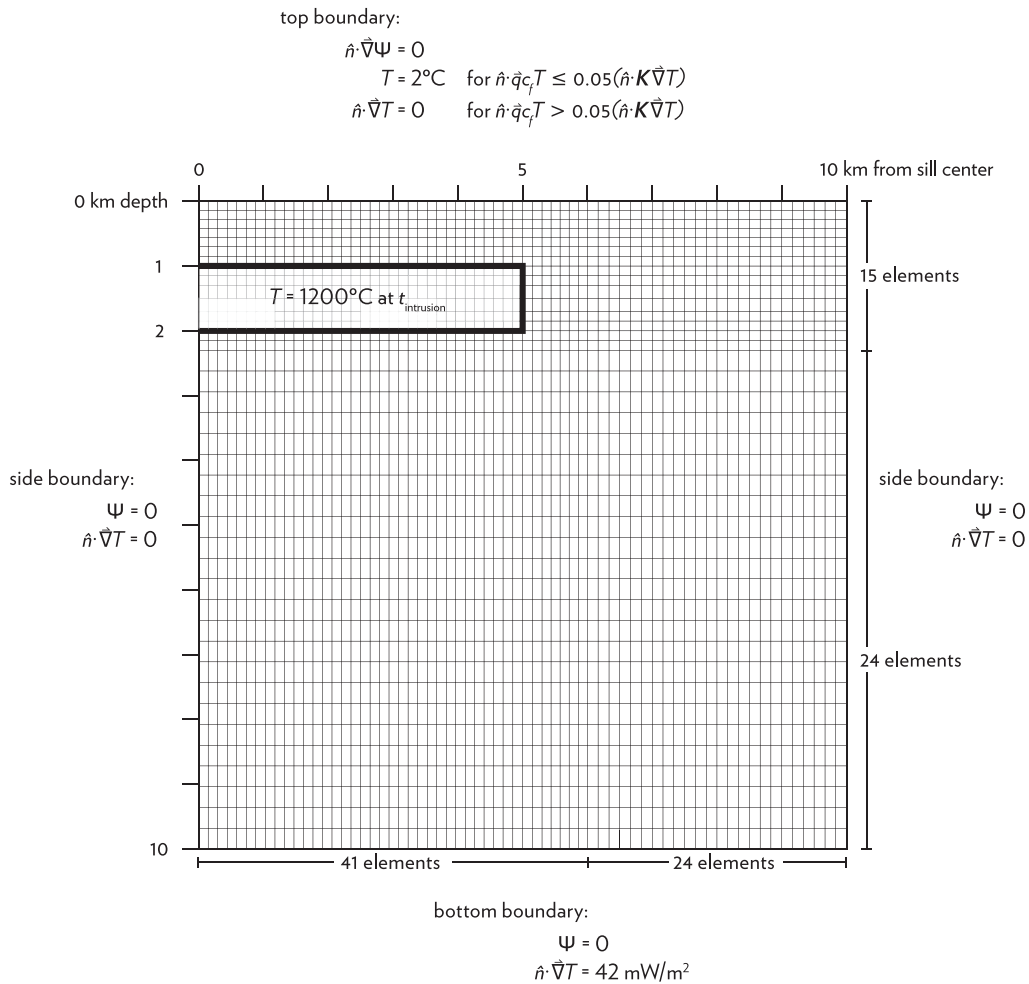


FIG. 1. Rectilinear grid used for the base case sill calculations. The finite element cells in the upper left quadrant are 146 m in the horizontal direction and 144 m in the vertical direction. In the upper right quadrant they are 167 × 144 m, in the lower left quadrant they are 146 × 308 m, and in the lower right quadrant they are 167 × 308 m.

surface at 21°C/km. Next, the sill is inserted by setting the temperature of the nodes within it to 1,200°C. A temperature gradient of 21°C may seem low for a volcanic region likely to be intruded by a sill. In fact, such a gradient may be high—pore water convection driven by previous intrusive activity is likely to have cooled the area. For example, convection at the Galapagos Ridge has cooled adjacent areas (Fehn et al., 1983). The stream function is zero everywhere initially (no flow).

The base permeability of all rock strata (including the cooled sill) is homogeneous and isotropic. For most of our calculations we choose a base permeability of 10<sup>-15</sup> m<sup>2</sup> (1 md). This value was chosen because it appears to be appropriate for large-scale convective systems in basalt (Fehn et al., 1983) and is roughly compatible with measurements made in Ocean Drilling Program drill hole 504B (Anderson et al., 1985). Permeability in host rock near an intrusion departs from this base value for several reasons.

Permeability may decrease with depth as the increase in effective stress closes fractures. We do not take this into account in our models. Very hot magma will be impermeable because it cannot sustain open fractures. Thermal contraction where the sill cools may fracture it sufficiently that it becomes more permeable than its adjacent host (Lister, 1974). This increase in permeability associated with the “cracking front” is incorporated in our models by multiplying the base permeability by a temperature-dependent factor:

$$\frac{k}{k_0} = \begin{cases} 1 & T \leq 275^\circ\text{C} \\ 10^{0.02(T-275)} & 275 < T < 375 \\ 100 \times 10^{-0.02(T-375)} & T \geq 375. \end{cases} \quad (1)$$

This permeability dependence produces simulated venting temperatures that range from 350° to 400°C, similar to those observed at high-temperature hydrothermal vents at mid-ocean ridges (Von Damm et al., 1983; Cathles, 1993; Kelley et al., 2002). For most of the simulations, this permeability-temperature relationship is also applied in the host rock far away from the sill margins, because this immobilizes the hydrothermal plumes and allows the model system to vent large volumes of hot pore water at spatially isolated and discrete sites (i.e., possible ore deposits). The physical justification for the dependence of permeability on temperature is discussed below.

Since our goal is to address ore deposits, we display our results in terms of the amount of zinc metal vented into the ocean (and potentially accumulated as an ore deposit). The tonnage of zinc vented at each site is calculated assuming the venting solutions are saturated with zinc and that the total Zn solubility as chloride complexes in parts per million depends on temperature in degrees Celsius:

$$[\text{Zn}] = \begin{cases} e^{(-5.38784 + 0.0176T)} & T < 400^\circ\text{C} \\ 14.5 & T \geq 400. \end{cases} \quad (2)$$

This relation is similar to the one given by Large (1992) and applies to pore waters of approximately seawater salinity. The relationship dictates that convecting seawater is everywhere saturated with respect to zinc sulfide, and this requires that zinc be available for dissolution everywhere. The solubility

relationship is a simplification of reality but has a thermodynamically reasonable temperature dependence and is calibrated to vent chemistry data as shown in Figure 2. It is best thought of as a simple numerical way to connect fluid flow to metal transport and deposition. It allows us to show directly the consequences of heat and fluid mass transport for ore deposition.

### Modeling Results for Heuristic Cases

Figure 3 shows the simulated convective cooling of the base case sill shown in Figure 1. The sill cools to less than 250°C in 20,000 years. The most notable convection is the thermal plume that rapidly develops at the edge of the sill. This cell extracts much of the heat from the sill. Flow across the underside of the sill contributes heat and leached metals to the edge-cell discharge. The inflow of seawater over the top of the sill that moves horizontally across the sill to join the edge-cell upwelling produces horizontal temperature gradients near the sill axis that, at about 8,000 years after intrusion, produce a second upwelling plume near the sill axis.

The locations where hydrothermal plumes vent into the ocean remain relatively fixed in space. In particular, the edge cell moves left much more slowly than the cooling edge of the sill. The temperature dependence of permeability makes the first formed plumes more permeable, and they subsequently attract upwelling fluids to their location and are relatively immobile, although they progressively deviate from vertical (at 8,000 and 12,000 yr).

Figure 4 shows the total zinc transported across the sea floor through each boundary element. The calculation assumes the section is 3 km thick in the third dimension (an arbitrary number chosen to roughly match the spacing of the upwelling plumes). The bottom portion of the figure shows the locations and temperatures of the venting plumes through time. The edge plume reaches the surface and begins venting well before the interior plume reaches the surface. Hydrothermal venting starts just inside the edge of the sill at 2,100 years after intrusion; the interior cell starts 5,500 years later, at 8,200 years after intrusion. Venting at temperatures hotter than 300°C ceases in the edge plume ~10,000 years after it starts. The metal transported across the numerical sea floor is shown in the top part of the diagram. Slightly more

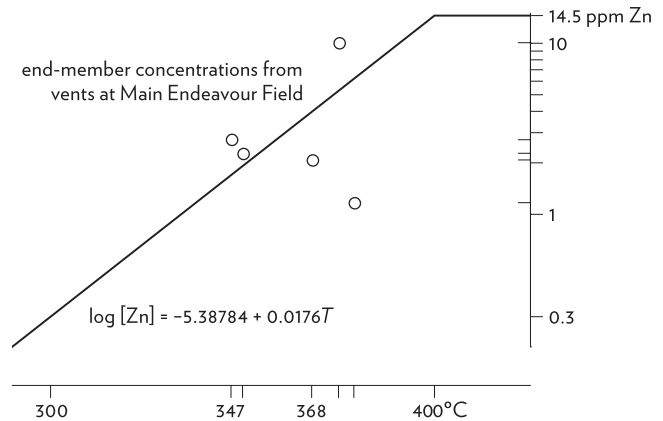


FIG. 2. The dependence of zinc solubility on temperature used in our modeling compared to the end-member concentrations derived from sea-floor observations (Seyfried et al., 2003).

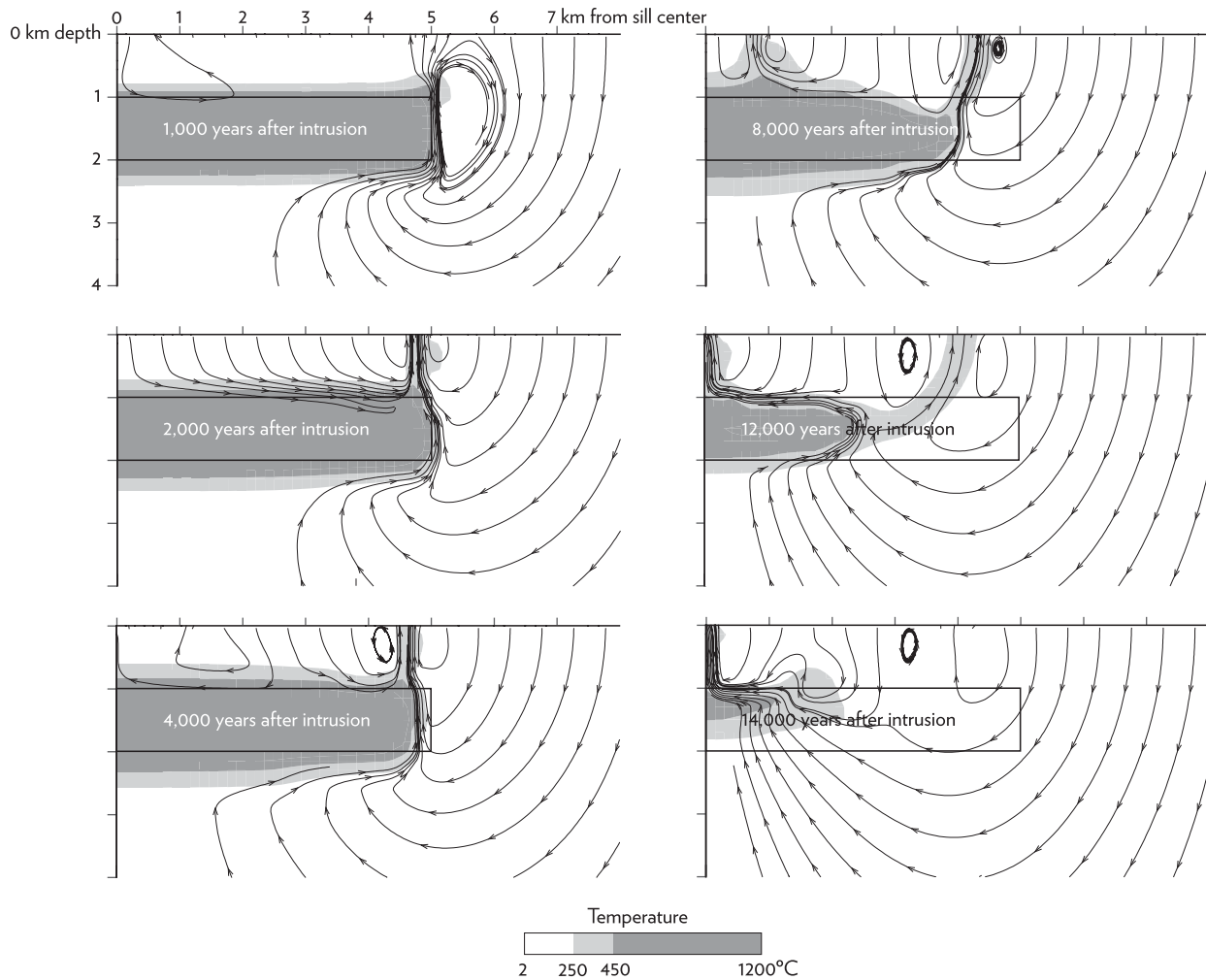


FIG. 3. Sill cooling simulation on grid shown in Figure 1. Streamlines with arrows indicate the pattern of fluid flow. Temperature is indicated by shading.

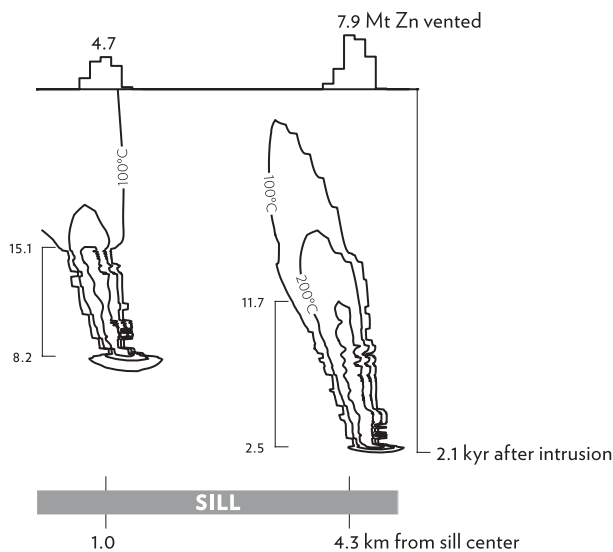


FIG. 4. Cumulative metal transport across the surface and temperature of venting through time for convection produced by the sill with the geometry shown in Figure 1.

metal is vented from the edge vent (7.9 vs. 4.7 Mt). Comparison of the temperature and metal diagrams shows that, as expected, most metal is transported by fluids hotter than 300°C (i.e., the spatial range of the vented zinc coincides with that of >300°C venting). If uniformly extracted from the sill, the vented zinc would require the extraction of 57 ppm Zn from the sill in this case. Gabbro and basalt typically contain ~100 ppm Zn (Carmichael, 1982).

The case in which permeability only follows equation (1) in the sill elements and is constant in the host rock is shown in Figure 5. With the host permeability independent of temperature, a single edge plume sweeps smoothly toward the center with time. Weak mineralization is spread over a broad area (although a comparable amount of zinc metal is vented) and spatially discrete metal deposits are not formed. The total amount of metal vented to the ocean is slightly less than the previous case, because the more focused plumes lose less heat warming host rock. This is more evident when comparing the evolution of the total energies of the systems through time. Figure 6 shows how the heat introduced by the sill is removed from the domain by advection of fluids hotter than 300°C. The permeability-focused convection is 12 percent

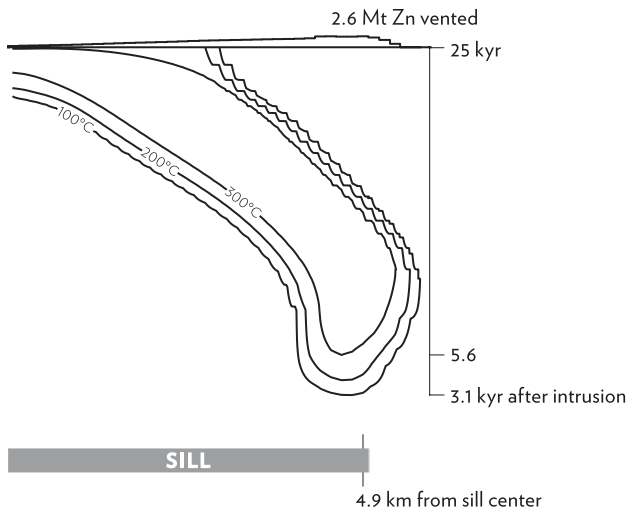


FIG. 5. Cumulative metal transport across the surface and temperature of venting through time for the case with the geometry of Figure 1 and the same parameters as in Figure 4, except that permeability is a function of temperature in the sill only and constant everywhere else.

more efficient than the convection without the positive feedback between temperature and permeability in the host surrounding the sill.

If the sill is twice as long (a 10-km half-sill), the simulation produces venting as shown in Figure 7. Venting at the edge begins at the same time as in the 5 km case; the second plume also begins about 5,500 years later but lasts longer, because more heat is available in the longer sill. A third and abortive fourth plume form and begin surface venting with a similar (5,500 yr) delay.

Host permeability affects the number of vents, how soon they form after intrusion, and the total amount of metal transported across the model sea floor. This is shown in Figure 8. At lower host permeability, thermal plumes above a sill buried to 1 km depth take longer to reach the surface because the

convective pore water flux is smaller and the thermal fronts move more slowly. The amount of zinc metal transported across the sea floor is maximized when the host permeability is  $10^{-15} \text{ m}^2$  (1 millidarcy). It is less at lower host permeability because the sill takes longer to cool and the conductive heat loss is greater. For a host permeability of  $10^{-16} \text{ m}^2$  (not shown), the sill cools entirely by conduction; there is no thermal venting and no zinc transport across the sea floor. Zinc transport across the sea floor is less at permeabilities greater than  $10^{-15} \text{ m}^2$  because more plumes form and more heat is lost in warming the host rock above the sill (see also Hayba and Ingebritsen, 1997), and there is more entrainment of cold seawater. The loss of heat and cooler venting disproportionately affects zinc transport because metal solubility in our models depends exponentially on temperature. As host permeability increases, an increasing fraction of the metal resources of the numerical district is contained in a few deposits among many. This kind of distribution in real systems may therefore suggest a relatively high host permeability.

Sill depth also affects hydrothermal venting and metal transport, as shown in Figure 9. Calculations were carried out for 1-km-thick, 5-km half-width sills emplaced such that their tops lie at depths of 1, 2, 4, and 8 km. The metal transport across the sea floor decreases as the depth of the sill increases because the fraction of sill heat vented by fluids hotter than  $300^\circ\text{C}$  decreases (see Fig. 9). The thermal plume takes about twice as long to reach the seafloor with each doubling of sill depth. This is expected because the circulation rate (mass flux) depends only on the permeability and the temperature difference across the thermal convection layer (Cathles, 1981), so the arrival time is linearly related to sill depth. As sill depth increases, convection at the sill edge becomes increasingly dominant. In the 8-km case, a hot plume never reaches the surface.

**The Bell River Sill at the Matagami VMS District**

The Matagami VMS district has been mined since the early 1960s and exploration has continued to the present. Figures

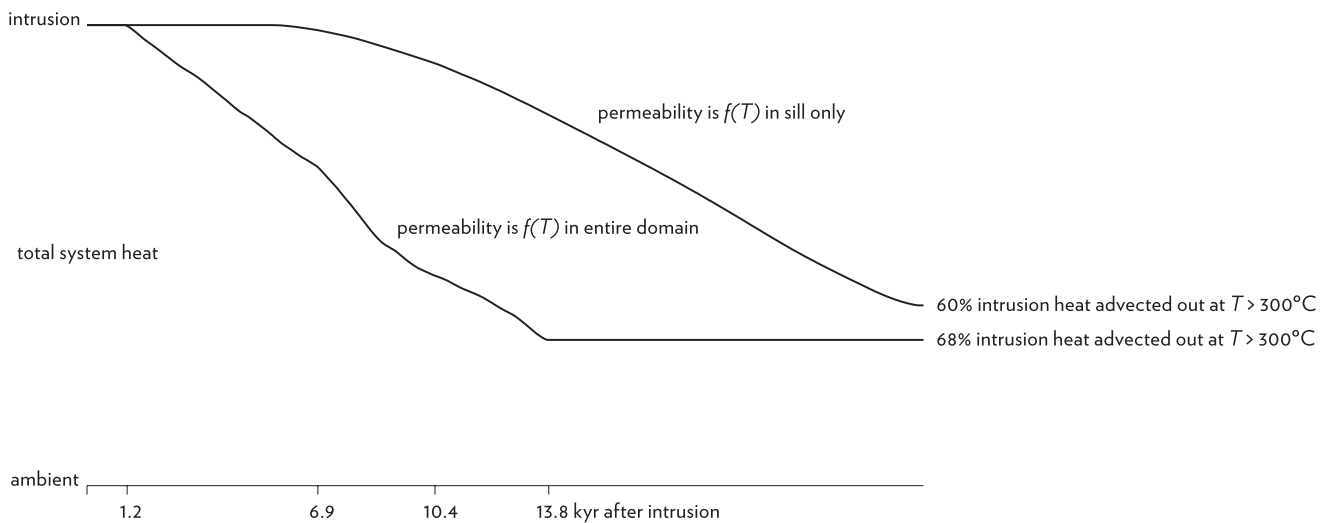


FIG. 6. Cumulative heat lost through the top boundary by advection of fluids hotter than  $300^\circ\text{C}$  for the cases shown in Figures 4 and 5. System heat is normalized to the heat added by the intrusion, assuming the width of the sill perpendicular to the section is 3 km. The total heat added by the intrusion is  $7.2 \times 10^{19} \text{ J}$ .

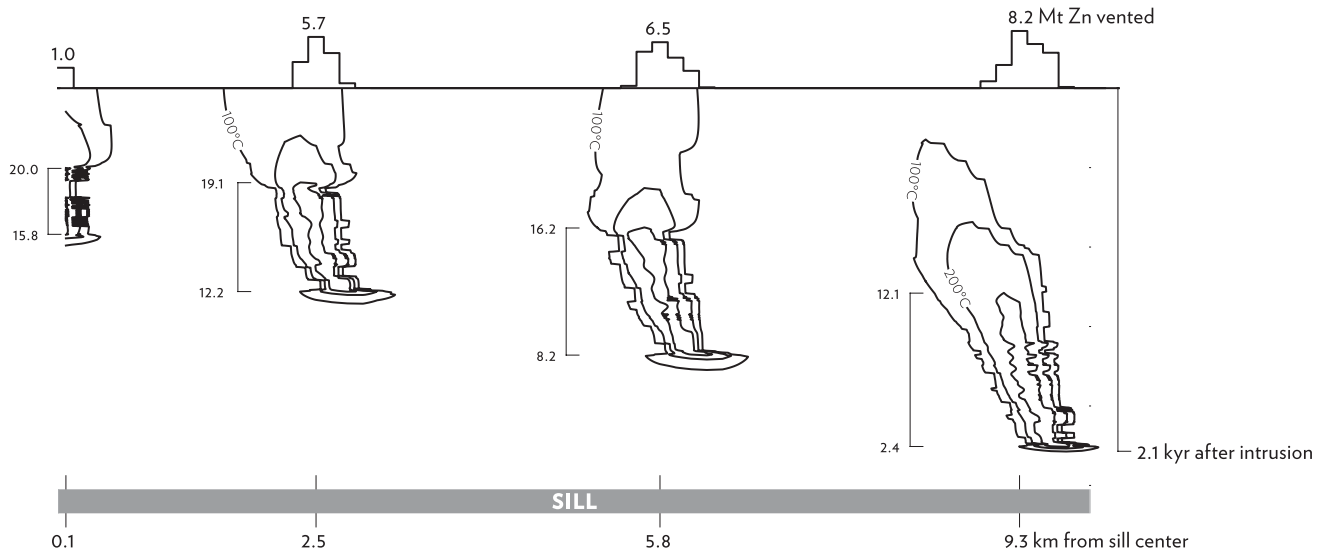


FIG. 7. Metal transport across the surface (upper portion) and temperature of venting through time (lower portion) for the case identical to Figure 1 but twice as long in the horizontal direction (half-sill is 10 km long; domain is 20 km). The grid spacing is adjusted to keep element sizes the same.

10 (map view) and 11 (cross section A-A') show the geology at Matagami, simplified to highlight the sill and overlying rocks extruded contemporaneously. Most of the deposits are conformable with the Key Tuffite, a silicified tuff with a thickness ranging from 0.3 to 20 m (Liaghat and MacLean, 1992). The footwall units below the ore horizon include the Watson Lake Rhyolite and the Bell River Complex intrusion. Both have U-Pb whole zircon dates of ~2724 Ma (Mortensen, 1993), and the Bell River Complex is considered to be the heat source which drove hydrothermal circulation that created the ore deposits (Maier et al., 1996). The Key Tuffite is overlain primarily by intermediate to mafic volcanics, beginning with the Wabasse Group basalts. Upsection are some interfingering rhyolites and small tuffaceous units, followed by hundreds of meters of massive basalt.

Some metal was deposited in the hanging wall associated with intermittent tuffite units within 200 m up stratigraphy from the Key Tuffite. A small, 32-kt deposit at the nose of the anticline is in hanging-wall strata. Some of the deposits on the south limb of the anticline have sulfide zones that extend 100 m above the main orebodies (Lavallière et al., 1994). These features have textures and relationships with upper tuffite units which indicate subsea-floor deposition. Recent discoveries farther southwest represent significant ore deposition up to 200 m in synvolcanic hanging-wall strata (G. Roy and R. Nieminen, pers. commun.).

The greatest number of deposits, however, have been discovered where the Key Tuffite lies near the surface. Clusters of deposits are located on the north and south limbs of the major regional anticline shown and to the west where the

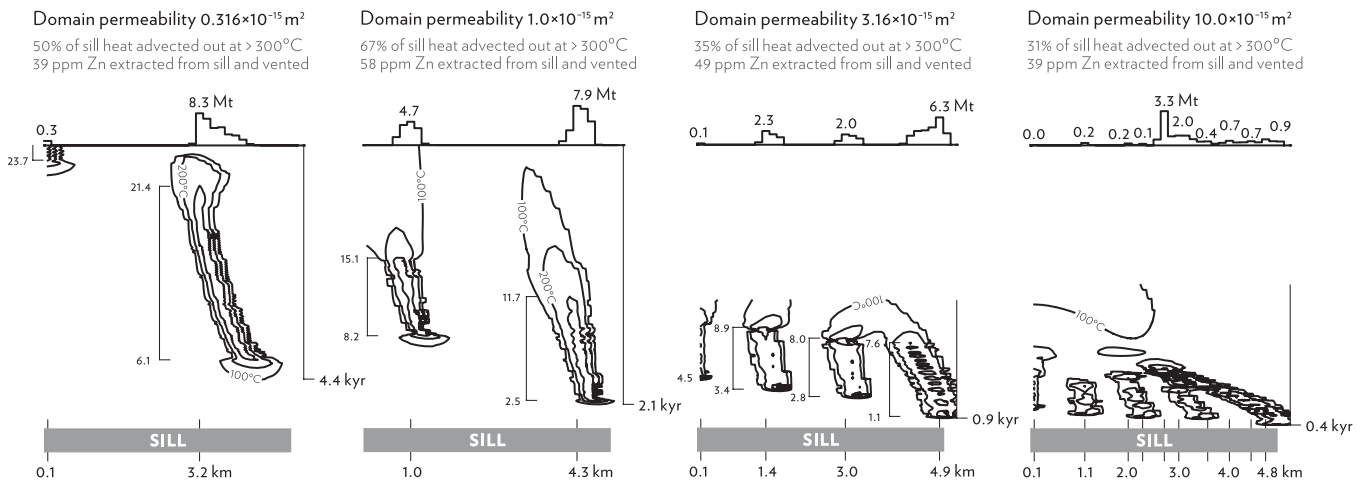


FIG. 8. Cumulative tons of zinc vented from each element across the top boundary (upper portions) and temperature of fluids venting as a function of time (lower portions) for cases with different base permeabilities. The sill top is at 1 km depth, as in Figure 1. The time step for each case is adjusted to keep the Courant number less than 1.

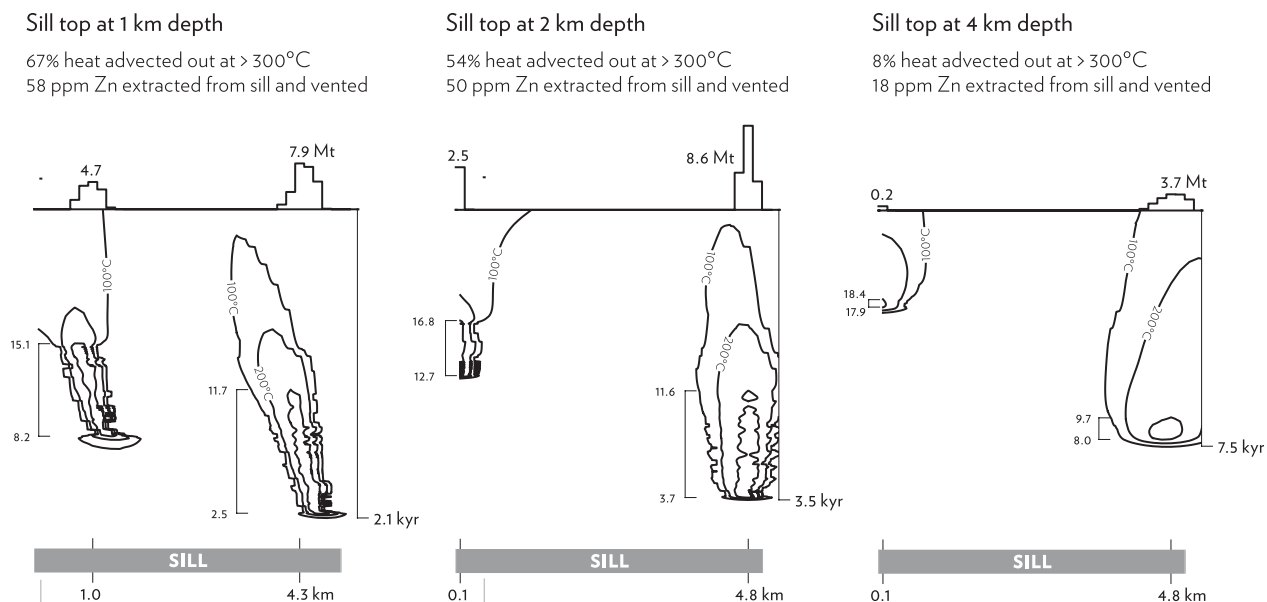


FIG. 9. Cumulative tons of zinc vented from each element across the top boundary (upper portions) and temperature of fluids venting as a function of time (lower portions) for cases with the intrusion at different depths. Permeability is  $10^{-15} \text{ m}^2$  and the time step is 50 years in all cases. The grid is modified as described in the text.

same units crop out again. The north limb has six deposits, which together contain 0.51 Mt of zinc metal; the south limb has seven deposits with 4.8 Mt of zinc metal; and the western area hosts four known deposits with 0.26 Mt of zinc metal.

Deposits almost certainly remain to be discovered between the south limb and the western areas, but the Key Tuffite lies at depths of up to 5 km, so exploration and mining will be costly.

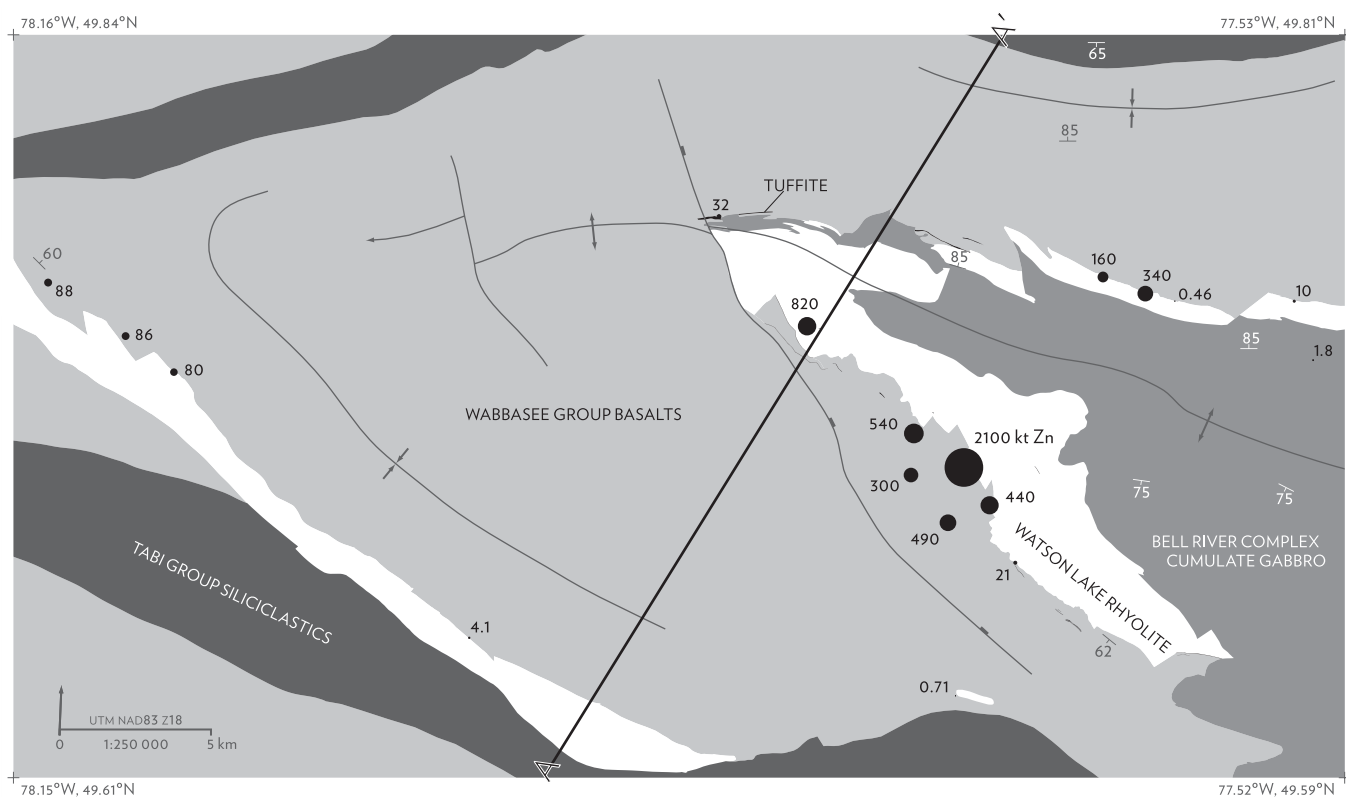


FIG. 10. Regional geology of the Matagami area (after Sharpe, 1968) showing the principal rock types, regional-scale structure, and tonnage of zinc metal at known deposits. Cross section A-A' is shown in Figure 11.

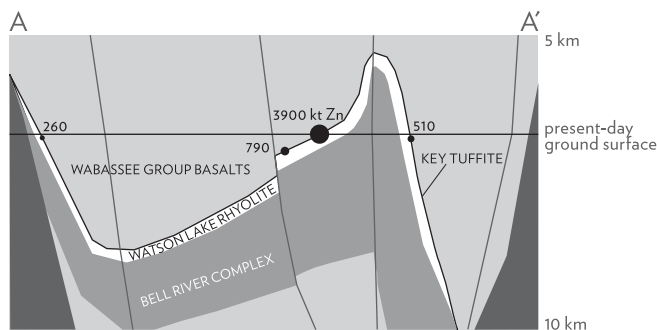


FIG. 11. Cross section A–A' from Figure 10. Zinc tonnages are summed from deposits projected onto the section.

Figure 12A shows the simulation domain: a reconstruction of cross section A–A' at the time of ore deposition, assuming conservation of rock volume and a sharp anticlinal postmineralization fold. The reconstructed sill reaches a maximum thickness of 6.5 km at its center and thins to a feather edge over 30 km. The top of the sill is flat. We calculate the pattern of hydrothermal and metal venting for this sill using the methods described above and assuming a host rock permeability of  $10^{-15} \text{ m}^2$ . The Matagami model differs from the previous models in one important regard, however. When the sill is intruded, the top of the Watson Lake Rhyolite is the top of the calculation domain. 100-m-thick increments of strata identical to the host rock are added starting 50,000 years after sill intrusion and continuing at intervals of 10,000 years thereafter. The temperature of each 100-m-thick stratum is the same as that of the sea floor ( $2^\circ\text{C}$ ) when it is deposited.

Figure 12B shows the metal vented and the temperature of venting. The vent sites have a fairly regular spacing of  $\sim 3.3$  km, slightly more than the expected free convection spacing of 2.7 km. The thermal plume at the far edge begins venting 700 years after sill intrusion, but dies quickly because the tapered edge contains little heat. Weak free-convection plumes develop above the central portion of the sill  $\sim 15,000$  years after intrusion, but most of the high-temperature venting occurs when the hot edge of the cooling sill sweeps across these vent sites (the shaded band labeled “spillage” on Fig. 12).

The tonnages of metal vented in the simulation have a spacing and a range of sizes similar to those of the VMS deposits discovered at Matagami. The modeled vent site 4.8 km from the sill center vents about ten times more metal than the vent site at the far edge (30.5 km from the sill center). This is similar to the observed distribution of metal at Matagami (3,900 kt on the south limb versus 260 kt in the western area). Any deposits between these two locations may be buried too deeply to have been discovered. Figure 13 shows how zinc is scavenged from the bottom as well as the top of the model sill.

Figure 14 shows how the modeled deposits compare to those discovered along the cross section A–A'. As in Figures 11 and 12, the discovered deposits at Matagami have been projected onto the section line. The shallow cluster of deposits on the south limb, which includes the 2,100 kt Matagami Lake mine (Fig. 10) and totals 3,900 kt of zinc metal, coincides with the modeled venting of 57.4 Mt zinc.

The metal tonnages in the model would be equal to the known tonnages if the zinc accumulation efficiency were  $\sim 7$  percent. Although it is difficult to assess depositional efficiency in sea-floor systems, the calculations in Converse et al. (1984) suggest that about 3 percent of sulfide particles vented will settle into a mound. If, as suggested in Lavallière et al. (1994), some sulfide material is precipitated below the sea floor, then 7 percent is not an unreasonable number. The cluster of known deposits with 790 kt zinc metal corresponds spatially to the modeled venting of 30.8 Mt. The modeled deposit would equal the known tonnages if about 3 percent of the metal in the model accumulated. The group of deposits near the edge of the sill with 260 kt of zinc metal are not reflected in the model; however, in this region, the error from estimating the reconstruction of the fold is at its maximum. If the western deposits correspond to the edge plume, where the model indicates venting of 5.8 Mt of zinc, the suggested depositional efficiency is about 4.5 percent.

### Discussion

One of the most interesting aspects of the simulations presented above is the way in which the convection cell that forms at the edge of the sill subsequently induces the formation of convection cells above the sill. The sequential formation of these cells is clearly shown in Figures 4 and 8 and especially in Figure 7. As discussed earlier, the sequential formation of the cells is caused by the horizontal temperature gradients that form adjacent to existing plumes. Seawater drawn down over the top of the sill by the edge cell creates the horizontal gradients that trigger the next cell inward, and so on. Because the cells that are formed above the still-hot sill are induced by horizontal gradients produced ultimately by the forced convection at the sill edge, they should all be considered forced convection cells rather than the free convection cells modeled by Lapwood (1948). In other words, none of these cells requires a critical Rayleigh number to be exceeded in order to form.

Another interesting aspect of the results is the decrease in the number of plumes that occur as sill burial depth is increased (Fig. 9). This dependence can be crudely understood in terms of the instability-wavelength dependence deduced by Lapwood (1948). His analysis showed that convection cells in an open, porous layer uniformly heated from below will have spacings between the upwelling plumes that are 2.7 times the layer thickness  $D$ , because thermal perturbations of this wavelength are the most unstable. This discharge spacing is physically logical because it is that which allows the convection cells to fit most easily into the layer (i.e., neither squashed nor stretched). If the natural “Lapwood spacing” of  $2.7D$  is much larger than the sill width, the sill will act as an isolated heat source and only one cell will form. As can be seen from Figure 9, this is the case for sills intruded at depths of 2 km or greater.

Similarly, the greater number of plumes formed above a sill buried by 1 km of host rock when the host permeability is increased (Fig. 8) can be understood if the Lapwood layer thickness is not the total physical distance to the sea floor, but the thickness of the thermal boundary layer over the sill when the cells form. The idea is that at higher permeabilities the critical Rayleigh number will be exceeded at thinner

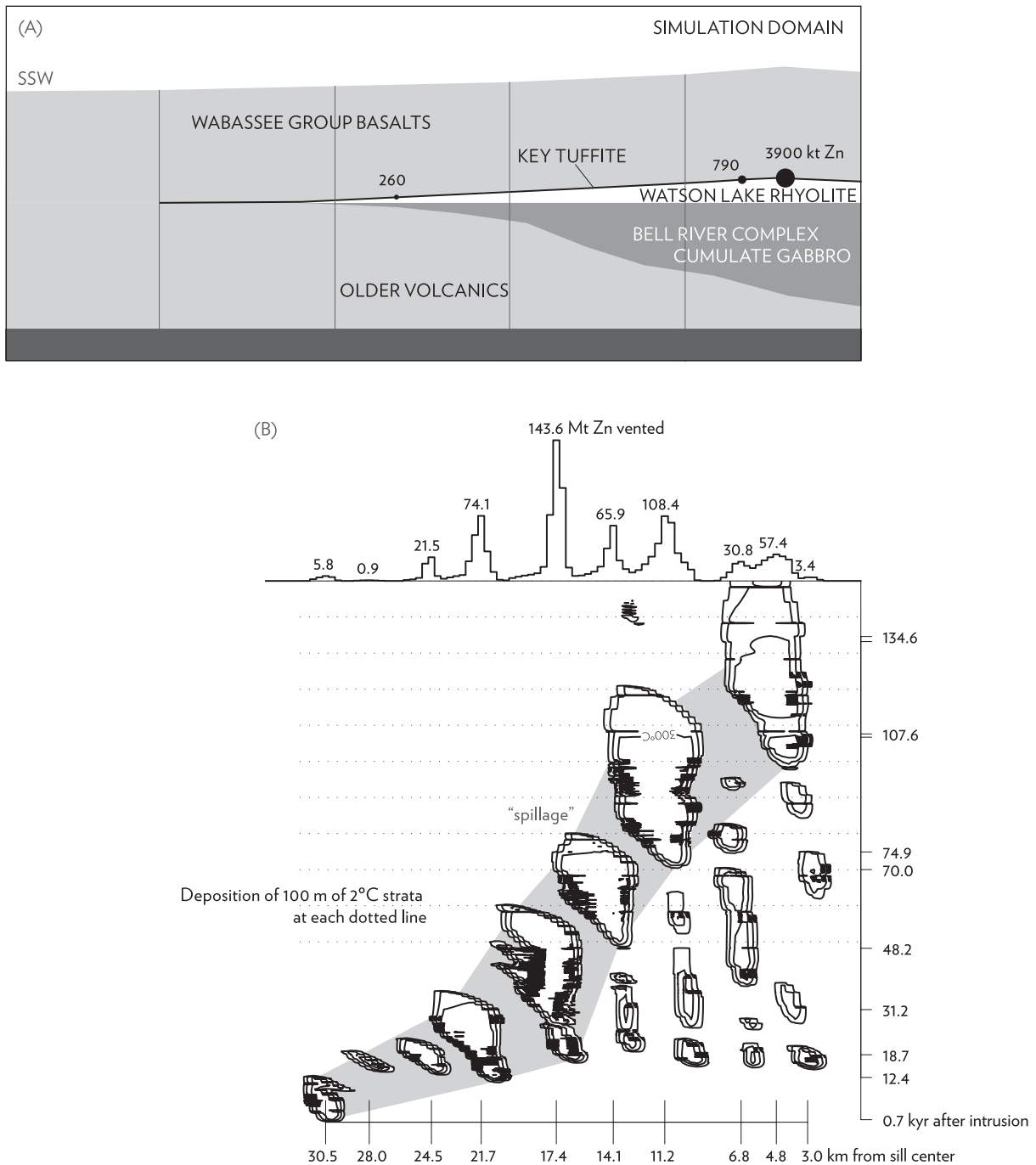


FIG. 12. The solution domain (A) and the cumulative tons of zinc and temperature of venting through time (B) for the Matagami simulation. Model grid spacing above the sill is 300 m × 150 m and the time step is 100 years, giving Peclet and Courant numbers of less than 5 and 1.5, respectively.

boundary layer thickness, and the spacing of the plumes will be less. We presume that, even though the cells may be induced by convection at the edge cell, the boundary layer thickness will still influence the spacing of the cells.

Assuming that the plumes rise at the same rate, the time between plume formation can be estimated by subtracting the times when venting starts for two plumes. The thermal boundary layer thickness can be computed for this time interval; it is equal to  $2\sqrt{Kt}$ , where  $K$  is the isotropic thermal

conductivity. The plume spacing will be ~2.7 times this distance. Table 1 shows that the plume spacing predicted on this basis is similar to that in the model simulations. The plume spacing thus seems to be related to the thickness of the thermal boundary layer at the time the plumes initiate and controlled by the physical ease with which the plumes fit within that thermal boundary layer.

The increase in permeability that we prescribe between 275° and 475°C is what locks the plumes in space and allows

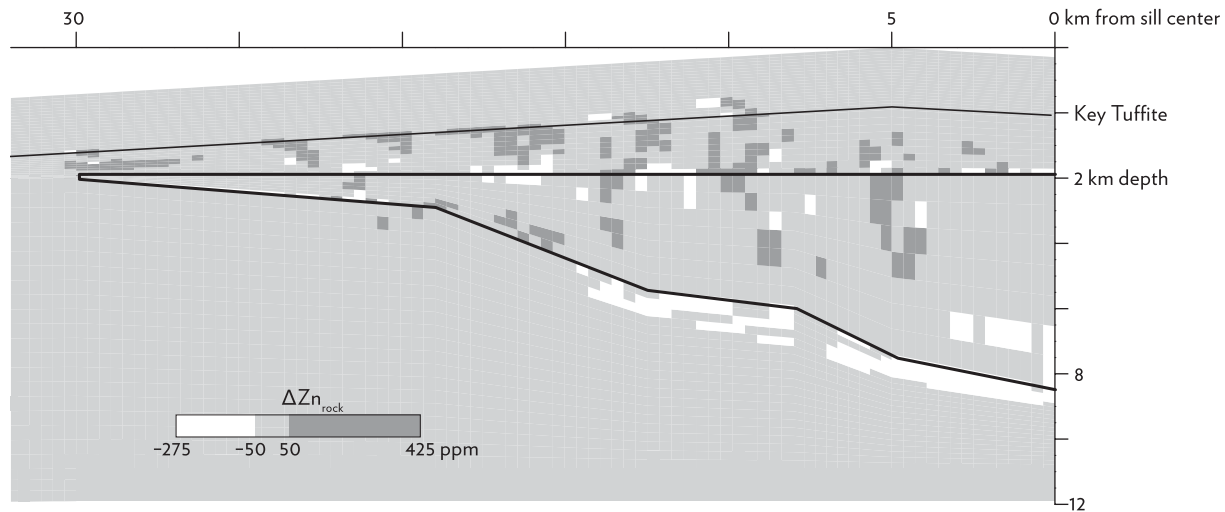


FIG. 13. Cumulative extraction and deposition of zinc at the end of the simulation. The algorithm is based on equation (2) and assumes local chemical equilibrium is maintained at all times.

the kind of sustained hydrothermal venting at the same location that allows discrete deposits to form. The decrease in permeability at higher temperatures has recently been discussed by Fourmier (1999). He argues that under hydrostatic conditions a barrier to flow will develop at  $\sim 400^\circ\text{C}$ , which coincides with the relatively high strain rate of the brittle-ductile transition. Cathles (1983) assumed a permeability decline starting at  $300^\circ\text{C}$  and attributed it to the healing of fractures by pressure dissolution of minerals where irregularities in their sides are in contact. The cause of the permeability decline at high temperature is similar but not of great importance to the issues we address here. What is of critical importance here is the augmented permeability at temperatures between  $275^\circ$  and  $475^\circ\text{C}$ , and especially its application to the host rock heated by hydrothermal convection.

Thermal contraction cracking provides a physical basis for increased rock permeability at  $\sim 350^\circ\text{C}$  within the sill. Permeability might subsequently decline as the rock becomes altered. Additionally, areas near an intrusion might be subject to minor deformation that would enhance permeability. Permeability might also be produced by fracturing associated with the rapid heating of pore waters when the sill is intruded. We do not consider these transient fluid volume changes that are short lived compared to the cooling time of the sill (see Appendix). Near the surface, extreme rock alteration could

increase rock permeability and lock discharge in place. The alteration at the Phelps Dodge mine at Matagami, for example, is estimated to have caused up to a 70 percent volume loss in the feeder pipes to the deposits (MacLean and Kranidiotis, 1987). This large volume loss could greatly increase the feeder pipe permeability. Feeder pipes typically extend hundreds of meters into the subsurface. For shallow sills, a combination of enhanced cracking where plumes originate at the top edge of the sill and enhanced permeability in the feeder pipes that develop where these plumes vent could be a sufficient explanation for the permeability-temperature dependence relation we have used. If so, our relation is imperfect mainly because it allows some migration of the hydrothermal plumes; in reality the greater cracking and alteration would make the sites of upwelling completely immobile.

For more deeply buried sills, stable plumes may require a permeable connection or some other way to immobilize hydrothermal upwelling from the sill to alteration pipes. The entrainment of cooler seawater could form an anhydrite selvage around the upwelling zones. Alternatively, flow from deep sills may simply have greater opportunity to find and utilize permeable fractures or faults, or deep sills may only vent hydrothermal fluids if a suitably placed permeable fracture is available. For uniform permeability of the host rock, a sill buried to 8 km will result in no venting of hydrothermal fluids (Fig. 9 and Discussion). The Kidd Creek deposit in Timmins,

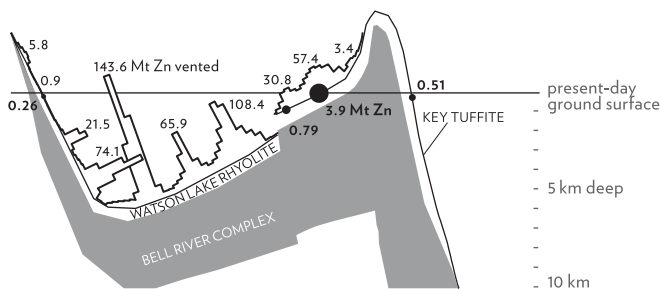


FIG. 14. The cumulative flux across the seafloor from Figure 12B folded back onto the Key Tuffite horizon from the cross section A-A' in Figure 11. Tonnages in bold are the known deposits from the camp.

TABLE 1. Simulated and Calculated Spacings for Permeability Cases

Permeability ( $10^{-15}$ m <sup>2</sup> )	Vent spacing (km)	Lapwood <sub>1km</sub> <sup>1</sup> (km)	TBL <sup>2</sup> (km)	Lapwood <sub>TBL</sub> <sup>3</sup> (km)
0.316	3.0	2.7	1.5	2.7
1	3.1	2.7	0.8	2.2
3.16	1.7	2.7	0.6	1.6
10	1.2	2.7	0.4	1.1

<sup>1</sup> Spacing of venting for a thermal layer with a thickness of 1 km

<sup>2</sup> Height of the thermal boundary layer

<sup>3</sup> Spacing of venting for a thermal layer with a thickness of the thermal boundary layer

Ontario, a giant VMS deposit that is the only deposit in its district, was successfully modeled as a consequence of sill intrusion at 13 km depth. But the hydrothermal upwelling had to be initiated with injection of rhyolite into a fracture connecting the sill to the deposit, and the fracture permeability had to be elevated to sustain convection in the fracture and produce the deposit (Barrie et al., 1999).

It is possible that upwelling could also be localized in permeable fractures over shallow sills. The pattern of fracture permeability rather than the physics of convection might control the spacing of deposits. Certainly, deposits are almost always associated with minor surface faults or fractures. This could be causative rather than opportunistic, but we do not think this is the case for two reasons. First, there would be no reason for the deposit spacing in our Matagami simulations (which contain no fractures) to so closely match the spacing of known deposits. Second, studies such as Fehn and Cathles (1979) show that fractures affect upwelling only if they are located very near to where the upwellings would occur in their absence.

We have immobilized upwellings from the sill with a plausible permeability-temperature dependence. It is possible that variations in other properties, such as the temperature dependence of water viscosity or density, could similarly immobilize the plumes. We have investigated this possibility by introducing a temperature-dependent fluid viscosity in the case shown in Figure 5 using functions based on Johnson and Norton (1991, their fig. 29). We find that this is not sufficient. The pressures in the system we simulate, assuming a water depth of 3 km, result in a temperature-viscosity function that is almost linear and decreases gradually. Plumes show no tendency to become fixed in space, and the venting pattern is very similar to that shown in Figure 5. Based on previous calculations (Cathles, 1983), the pressure and temperature dependence of pore water viscosity, density, and enthalpy will increase the efficiency of advective transport and decrease the cooling time of the sill. But these more realistic fluid properties will not immobilize the plumes; only changes in rock permeability appear capable of this.

We have ignored the latent heat of magma crystallization in our cooling calculations. This could increase the heat content of the sill by up to 30 percent (Norton and Cathles, 1979). High-temperature venting would be maintained for longer periods, and metal transport across the sea floor might be increased by 50 percent or more. This is a minor uncertainty compared to the zinc solubility function we have adapted, which could easily be increased or decreased by a factor of 3. The unusually high salinity of fluid inclusions of the south limb deposits (Ioannou et al., 2007) suggests the metal loading could be higher than we assume. As long as the salinity of the fluid is uniform, however, the convection pattern we simulate will remain valid within the limits of the Boussinesq approximation.

It should be noted that our modeled deposits form after a significant deposition of volcanic rocks on the model "ore horizon"—the sea floor at the time of sill intrusion. Because the hanging-wall deposition at Matagami is no more than 200 m above the Key Tuffite, this is an obvious discrepancy. The deposition of hanging-wall strata may be slower than we simulated, or the effective permeability in the real system may be

higher than we modeled. If the host permeability were greater, the large deposits would be expected to contain a greater fraction of the metal resource of the district (cf. Fig. 8).

There are a large number of factors that can affect deposit size that we have not considered. For example, change in the efficiency of metal deposition caused by ocean currents, local bathymetry, and other factors could be important. If the sill itself is tilted, simulations we have carried out show that hydrothermal venting near the upthrown end will be enhanced at the expense of venting over deeper portions of the sill. The topography of the top of the sill will produce horizontal temperature gradients that will tend to localize upwelling and produce larger deposits there. Subsurface permeability variations between rock units or due to differential fracturing of fault blocks could affect deposit size, as could major structure or faults, especially those that crosscut the direction of hydrothermal venting. The spacing could also be different in three dimensions.

Erendi (2000) has carried out 3-D simulations to evaluate this last possibility. These simulations show that a small, 1.75-km-thick sill 14 km in diameter intruded 2 km below the surface produces a single metal-rich deposit above the sill center. If this sill is tilted 15°, forced convection occurs along the base and top of the sill, and four vents form. Three times more metal is discharged through the vents located on the upper part of the sill. For a flat sill with twice the diameter, a dozen vents form and the vents are spaced 4 or 6 km apart. These vents are all concentric to the center, and there is no central vent.

The 3-D simulations should be taken only as an indicator of what the deposit spacing may be, because the Courant numbers for the smaller sill are at the limit of acceptability and are not acceptable for the larger sill. The vent spacings are, however, compatible with the 2-D simulations and with simple stability predictions (Lapwood, 1948, his table 4). The simulations suggest that if a sill is small, central, or updip deposits may be the largest. Especially if a sill is tilted, the drainage of hydrothermal fluids up its sides (top and bottom) is important in producing larger deposits. If the edges of an exposed sill are altered (suggesting substantial venting), paleo-updip locations should be considered especially prospective. In all cases, the deposit spacing appears to be quite robustly predicted by the depth of sill intrusion (for  $10^{-15}$  m<sup>2</sup> host permeability).

Considering the large number of factors that could affect deposit spacing, it is perhaps surprising that the spacing and size distribution of the deposits at Matagami were reasonably simulated by the models. The deposits calculated at the ends of the section shown in Figure 14 compare well with the tonnages of discovered deposits for reasonable accumulation efficiencies. The spacing of the modeled deposits along the numerical section agree well with those observed off-section at Matagami. This encourages the view that 3-D models that capture broad aspects of the geology and are progressively calibrated to mineralization and alteration data collected in an ongoing exploration program could be a useful component of that program. Modeling is now a part of the exploration process for petroleum resources and could eventually become a useful component of mineral exploration. For this to happen, a new generation of industrial-quality models needs to be developed and calibrated.

## Conclusions

VMS districts exhibit a remarkable regularity in deposit spacing and commonly contain one or two large deposits and a dozen or so smaller ones. We show that a simple and reasonable dependence of permeability on temperature localizes hydrothermal upwelling and produces a spatial pattern and range of vented fluid volumes similar to that found in VMS districts. The temperature dependence we employ (or some similar means to arrest the migration of hydrothermal venting) is required for the numerical simulations to produce discrete metal deposits. The largest metal resource in a district is produced by sills at an emplacement depth below 1 km of host rock with a permeability of  $10^{-15}$  m<sup>2</sup>. Tilted sills produce larger deposits on their upslope sides. The simulation of convective cooling of the flat-topped Bell River Complex at Matagami produces deposits with a spacing and size distribution similar to that observed among the known deposits. The localization of VMS deposits very near the "ore horizon" suggests that accumulation of hanging-wall strata is slower, or the permeability of the host rocks greater, at Matagami than we assume in the calculations. If the permeability of the host rocks is greater, the larger deposits will contain a greater fraction of the deposited metal. The success of the modeling in capturing broad aspects of deposit size and spacing suggests that properly calibrated 3-D models might be useful in a district exploration program and that only broad aspects of the geology (sill geometry and depth) need to be specified. In particular, faults and stratigraphic details may be opportunistically utilized and modify the locations of discharge sites and deposits only slightly.

## Acknowledgments

This material is based upon work supported by the National Science Foundation under grant 9811143 and by the Canadian Mining and Industry Research Organization (CAMIRO) under grant 96E01. Additional support for fieldwork at Matagami was provided by Noranda Exploration. We especially thank Grant Arnold, chief geologist at Noranda Exploration Matagami, for his encouragement, support of Pat Carr for two field seasons at Matagami, and geologic guidance. Thanks are also due to Paul Manhardt for maintenance of the solver core and coding support, and to Jenn Adams for aid with the convergence criteria. We thank Barb Dutrow and an anonymous reviewer for helpful suggestions which have greatly improved the manuscript.

January 15, June 20, 2008

## REFERENCES

- Anderson, M.P., and Woessner, W.W., 1992, Applied groundwater modeling: Simulation of flow and advective transport: San Diego, Academic Press, 381 p.
- Anderson, R.N., Zoback, M.D., Hickman, S.H., and Newmark, R.L., 1985, Permeability versus depth in the upper oceanic crust: In situ measurements in DSDP Hole 504B, eastern equatorial Pacific: *Journal of Geophysical Research*, v. 90, p. 3659–3669.
- Baker, A.J., 1983, Finite element computational fluid mechanics: New York, Hemisphere, 508 p.
- Baker, A.J., and Kim, J.W., 1987, A Taylor weak statement for hyperbolic conservation laws: *International Journal of Numerical Methods*, v. 7, p. 489–520.
- Baker, A.J., and Soliman, M.O., 1983, A finite-element algorithm for computational fluid dynamics: *American Institute of Aeronautics and Astronautics Journal*, v. 21, p. 816–827.
- Barrie, C.T., Cathles, L.M., Erendi, A.E., Schwaiger, H., and Murray, C., 1999, Heat and fluid flow in VMS-forming hydrothermal systems: Reviews in *Economic Geology*, v. 8, p. 201–219.
- Brikowski, T., and Norton, D., 1989, Influence of magma chamber geometry on hydrothermal activity at mid-ocean ridges: *Earth and Planetary Science Letters*, v. 93, p. 241–255.
- Carmichael, R.S., 1982, Handbook of physical properties of rocks: Boca Raton, CRC Press, 404 p.
- Cathles, L.M., 1977, An analysis of the cooling of intrusives by ground-water convection which includes boiling: *ECONOMIC GEOLOGY*, v. 72, p. 804–826.
- , 1978, Hydrodynamic constraints on the formation of Kuroko deposits: *Mining Geology*, v. 28, p. 257–266.
- , 1981, Fluid flow and genesis of hydrothermal ore deposits: *ECONOMIC GEOLOGY 75<sup>TH</sup> ANNIVERSARY VOLUME*, p. 424–457.
- , 1983, An analysis of the hydrothermal system responsible for massive sulfide deposition in the Hokuroku basin of Japan: *ECONOMIC GEOLOGY MONOGRAPH* 5, p. 439–487.
- , 1993, A capless 350°C flow zone model to explain megaplumes, salinity variations, and high-temperature veins in ridge axis hydrothermal systems: *ECONOMIC GEOLOGY*, v. 88, p. 1977–1988.
- , 1997, Thermal aspects of ore formation, in Barnes, H.L., ed., *Geochemistry of hydrothermal ore deposits*, 3rd ed.: New York, Wiley, p. 192–227.
- Cheng, P., and Minkowycz, W.J., 1977, Free convection about a vertical flat plate embedded in a porous medium with application to heat transfer from a dike: *Journal of Geophysical Research*, v. 82, p. 2040–2044.
- Cheng, P., and Pop, I., 1984, Transient free convection about a vertical flat plate embedded in a porous medium: *International Journal of Engineering Science*, v. 22, p. 253–264.
- Christensen, N.I., and Salisbury, M.H., 1985, Seismic velocities, densities, and porosities of Layer 2B and Layer 2C Basalts from Hole 504B: Initial Reports of the Deep Sea Drilling Project, v. 83, p. 367–375.
- Clauser, C., and Huenges, E., 1995, Thermal conductivity of rocks and minerals, in Ahrens, T.J., ed., *Rock physics and phase relations: A handbook of physical constants*: Washington, D.C., American Geophysical Union, AGU Reference Shelf 3, p. 105–126.
- Converse, D.R., Holland, H.D., and Edmond, J.M., 1984, Flow rates in the axial hot springs of the East Pacific Rise (21°N): implications for the heat budget and the formation of massive sulfide deposits: *Earth and Planetary Science Letters*, v. 69, p. 159–175.
- Daus, A.D., Frind, E.O., and Sudicky, E.A., 1985, Comparative error analysis in finite element formulations of the advection-dispersion equation: *Advances in Water Resources*, v. 8, p. 86–95.
- Erendi, A.H., 2000, Computer simulation of geological processes: Unpublished Ph.D. thesis, Ithaca, New York, Cornell University, 348 p.
- Fehn, U., and Cathles, L.M., 1979, Hydrothermal convection at slow-spreading mid-ocean ridges: *Tectonophysics*, v. 55, p. 239–260.
- Fehn, U., Green, K.E., Von Herzen, R.P., and Cathles, L.M., 1983, Numerical models for the hydrothermal field at the Galapagos spreading center: *Journal of Geophysical Research*, v. 88, p. 1033–1048.
- Fournier, R.O., 1999, Hydrothermal processes related to movement of fluid from plastic into brittle rock in the magmatic-epithermal environment: *ECONOMIC GEOLOGY*, v. 94, p. 1193–1212.
- Gibson, H.T., and Watkinson, D.H., 1990, Volcanogenic massive sulphide deposits of the Noranda cauldron and shield volcano, Quebec, in Rive, M., Verpaest, P., Gagnon, Y., Lulin, J.M., Riverin, G., and Simard, A., eds., *The northwestern Quebec polymetallic belt: A summary of 60 years of mining exploration*: Canadian Institute of Mining and Metallurgy, p. 119–132.
- Hayba, D.O., and Ingebritsen, S.E., 1997, Multiphase groundwater flow near cooling plutons: *Journal of Geophysical Research*, v. 102, p. 12,235–12,252.
- Ioannou, S.E., Spooner, E.T.C., and Barrie, C.T., 2007, Fluid temperature and salinity characteristics of the Matagami volcanogenic massive sulfide district, Quebec: *ECONOMIC GEOLOGY*, v. 102, p. 691–715.
- Johnson, J.W., and Norton, D., 1991, Critical phenomena in hydrothermal systems: State, thermodynamic, electrostatic, and transport properties of H<sub>2</sub>O in the critical region: *American Journal of Science*, v. 291, p. 541–648.
- Kelley, D.S., Baross, J.A., and Delaney, J.R., 2002, Volcanoes, fluids, and life at mid-ocean ridge spreading centers: *Annual Review of Earth and Planetary Sciences*, v. 30, p. 385–491.
- Lapwood, E.R., 1948, Convection of a fluid in a porous medium: *Mathematical Proceedings of the Cambridge Philosophical Society*, v. 44, p. 508–521.
- Large, R.R., 1992, Australian volcanic-hosted massive sulfide deposits: Features, styles and genetic models: *ECONOMIC GEOLOGY*, v. 87, p. 471–510.

- Lavallière, G., Guha, J., and Daigneault, R., 1994, Cheminées de sulfures massifs atypiques du gisement d'Isle Dieu, Matagami, Québec: implications pour l'exploration: *Exploration and Mining Geology*, v. 3, p. 109–129.
- Liaghat, S., and MacLean, W.H., 1992, The Key Tuffite, Matagami mining district: Origin of the tuff components and mass changes: *Exploration and Mining Geology*, v. 1, p. 197–207.
- Lister, C.R.B., 1974, On the penetration of water into hot rock: *The Geophysical Journal of the Royal Astronomical Society*, v. 39, p. 465–509.
- MacLean, W.H., and Kranidiotis, P., 1987, Immobile elements as monitors of mass transfer in hydrothermal alteration: Phelps Dodge massive sulfide deposit, Matagami, Quebec: *ECONOMIC GEOLOGY*, v. 82, p. 951–962.
- Maier, W.D., Barnes, S.J., and Pellet, T., 1996, The economic significance of the Bell River Complex, Abitibi subprovince, Quebec: *Canadian Journal of Earth Science*, v. 33, p. 967–980.
- Manning, R.A., Manhardt, P.D., Orzechowski, J.A., Cathles, L.M., and Baker, A.J., 1993, A parallel 3-D geologic basin modeling code: Technical Report for the SIAM Conference on Mathematical and Computational Issues in the Geosciences, Knoxville, Tenn., Computational Mechanics Corporation.
- Mortensen, J.K., 1993, U-Pb geochronology of the eastern Abitibi subprovince, part 1: Chibougamau-Matagami-Joutel region: *Canadian Journal of Earth Sciences*, v. 30, p. 11–28.
- Norton, D., and Knight, J., 1977, Transport phenomena in hydrothermal systems: Cooling plutons: *American Journal of Science*, v. 277, p. 937–981.
- Norton, D.L., and Cathles, L.M., 1979, Thermal aspects of ore deposition, *in* Barnes, H.L., ed., *Geochemistry of hydrothermal ore deposits*: New York, Wiley, p. 611–631.
- Parmentier, E.M., 1979, Two phase natural convection adjacent to a vertical heated surface in a permeable medium: *Journal of Heat and Mass Transfer*, v. 22, p. 849–855.
- Rosenberg, N.D., Spera, F.J., and Haymon, R.M., 1993, The relationship between flow and permeability field in seafloor hydrothermal systems: *Earth and Planetary Science Letters*, v. 116, p. 135–153.
- Shardt, C., Yang, J., and Large, R., 2005, Numerical heat and fluid-flow modeling of the Panorama volcanic-hosted massive sulfide district, Western Australia: *ECONOMIC GEOLOGY*, v. 100, p. 547–566.
- Seyfried, W.E., Jr., Seewald, J.S., Berndt, M.E., Ding, K., and Foustoukos, D.I., 2003, Chemistry of hydrothermal vent fluids from the Main Endeavour Field, northern Juan de Fuca Ridge: Geochemical controls in the aftermath of June 1999 seismic events: *Journal of Geophysical Research*, v. 108, p. 2429.
- Sharpe, J.I., 1968, Geology and sulfide deposits of the Matagami area, Abitibi-East County: Geological Report 137, Ressources Naturelles Québec, 122 p.
- Tanimura, S., Date, J., Takahashi, T., and Ohmoto, H., 1983, Stratigraphy and structure of the Hokuroku district: *ECONOMIC GEOLOGY MONOGRAPH* 5, p. 24–39.
- Trubitsyn, V.P., Nikolaichik, V.V., and Jacoby, W.R., 1993, A study of hydrothermal convection in saturated porous media: *Tectonophysics*, v. 217, p. 73–89.
- Turcotte, D.L., and Schubert, G., 1982, *Geodynamics: Applications of continuum physics to geological problems*: New York, Wiley, 450 p.
- Von Damm, K.L., Grant, B., and Edmond, J.M., 1983, Preliminary report on the chemistry of hydrothermal solutions at 20°North, East Pacific Rise, *in* Rona, P.A., Bostrom, K., and Smith, K.L., Jr., eds., *Hydrothermal processes at seafloor spreading centers*: New York, Plenum, p. 369–389.

## APPENDIX

## Theoretical Foundations

The simulations reported here are based on finite element solutions to the equations for the conservation of energy (heat transport):

$$\rho_m c_m \frac{\partial T}{\partial t} = -\vec{\nabla} \cdot \vec{q} c_f T + \vec{\nabla} \cdot (\mathbf{K} \vec{\nabla} T) \quad (\text{A1})$$

and for the conservation of fluid mass and momentum expressed as a vorticity equation in two dimensions:

$$0 = \vec{\nabla} \cdot \frac{1}{k} \vec{\nabla} \Psi + \frac{g}{v_f} \frac{\partial \rho_f}{\partial z} \quad (\text{A2})$$

or three dimensions:

$$0 = \vec{\nabla} \cdot \frac{1}{k} \vec{\nabla} \Psi_1 - \vec{\nabla} \cdot \frac{1}{k_1} \frac{\partial \vec{\Psi}}{\partial x} - \frac{g}{v_f} \frac{\partial \rho_f}{\partial z}$$

$$0 = \vec{\nabla} \cdot \frac{1}{k} \vec{\nabla} \Psi_1 - \vec{\nabla} \cdot \frac{1}{k_1} \frac{\partial \vec{\Psi}}{\partial y}$$

$$0 = \vec{\nabla} \cdot \frac{1}{k} \vec{\nabla} \Psi_1 - \vec{\nabla} \cdot \frac{1}{k_1} \frac{\partial \vec{\Psi}}{\partial z} - \frac{g}{v_f} \frac{\partial \rho_f}{\partial x}$$

where the stream function  $\vec{\Psi}$  is defined such that its curl is the mass flux:

$$\vec{\nabla} \times \vec{\Psi} \equiv \vec{q} \quad (\text{A3})$$

(in two dimensions  $\Psi$  is a scalar field). Parameters are defined in Table A1. The equations are standard and are discussed in

TABLE A1. Model Parameters

Property	Symbol	Initial Value
Rock matrix		
Fracture porosity <sup>1</sup>	$\phi$	0.01
Density	$\rho_m$	$2.9 \times 10^3 \text{ kg/m}^3$
Heat capacity	$c_m$	$800 \text{ J/kg}^\circ\text{C}$
Isotropic permeability <sup>2</sup>	$k_0$	$10^{-15} \text{ m}^2$
Isotropic thermal conductivity <sup>3</sup>	$K$	$2 \text{ J/m/s}^\circ\text{C}$
Sill temperature		$1,200^\circ\text{C}$
Pore fluid		
Mass flux	$\vec{q}$	$\text{kg/m}^2$
Kinematic viscosity <sup>4</sup>	$v_f$	$2.0 \times 10^{-7} \text{ m}^2/\text{s}$
Fluid density	$\rho_f^0$	$\rho_f = \rho_f^0 - \alpha_f T$
Fluid density at $20^\circ\text{C}$	$\rho_f$	$10^3 \text{ kg/m}^3$
Coeff. of thermal expansion	$\alpha_f$	$10^{-3} \text{ } 1/^\circ\text{C}$
Heat capacity	$c_f$	$4 \times 10^3 \text{ J/kg}^\circ\text{C}$
Longitudinal dispersion	$\alpha_L$	$30 \text{ m}$
Transverse dispersion	$\alpha_T$	$10 \text{ m}$
Global		
Acceleration due to gravity	$g$	$9.8 \text{ m/s}^2$

<sup>1</sup> Christensen and Salisbury, 1985

<sup>2</sup> Anderson et al., 1985

<sup>3</sup> Clauser and Huenges, 1995

<sup>4</sup> This value is typical for  $T \geq 100^\circ\text{C}$

many publications (e.g., Turcotte and Schubert, 1982; Cathles, 1997). The Helmholtz theorem is used to separate divergent and nondivergent flows, and equation (A2) describes the nondivergent flow. Thus, pressure transients caused by the thermal expansion of rock and fluid when the sill is intruded are ignored in our simulations. For  $k > 0.316 \times 10^{-15} \text{ m}^2$ , these transients are of short duration compared to the time required for the sill to convectively cool.

The equations are solved subject to the initial conditions in Table A1 and the boundary conditions given in Figure 1. The initial temperature is set to a normal thermal gradient of  $\sim 20^\circ\text{C}/\text{km}$ , and the  $1,200^\circ\text{C}$  sill is superimposed. Boundary conditions are no flow out the bottom and sides of the simulation domain and free flow out the top. Temperature boundary conditions are insulating sides, normal heat flow across the bottom, and either a constant temperature top or zero thermal gradient across the top if venting is relatively rapid.

Equations (A1–A3) are solved using standard finite element techniques (Baker, 1983; Baker and Soliman, 1983; Baker and Kim, 1987) on rectilinear mesh using a code called BasinLab (Manning et al., 1993). Matrix inversion of the temperature equation uses the generalized minimal residual with an incomplete L-U factorization preconditioner. Gaussian elimination is used to invert the finite element equations for the stream function and mass flux equations.

Numerical convergence of the advective-dispersive temperature equation is an important consideration. Convergence is assured if the dimensionless grid cell Peclet number is less than  $\sim 2$  (Daus et al., 1985):

$$Pe = \frac{\rho_m c_m q_y \Delta y}{\rho_f (\alpha_L c_f q_y + K_y)} < 2, \quad (\text{A4})$$

and the Courant number is less than  $\sim 1$  (Anderson and Woessner, 1992):

$$C = q_y \frac{\rho_f c_f \Delta t}{\rho_m c_m \Delta y} < 1. \quad (\text{A5})$$

Adequate convergence is possible at larger grid spacings and time steps (Anderson and Woessner, 1992). This is important because grid spacing and time step control how long a simulation takes to perform on a computer.

Figure A1 shows the cumulative metal transport across the top surface and the vent positions and temperatures through time for the sill shown in Figure 1 at successively refined grids and time steps. The grid is coarsened by increasing all of the element sizes in the computational domain by roughly the same factor. The label  $\Delta y$  gives the vertical spacing of the elements in the quadrant above and in the sill, where mass fluxes are the highest and therefore the simulation most prone to error. The mass flux used in the calculations is  $30 \text{ kg/m/yr}$ , the observed maximum from the simulations.

The most refined case (leftmost on Fig. A1) took approximately a week on a lightly shared SGI Octane. Through successive coarsenings (not shown), the case with  $\Delta y$  of  $150 \text{ m}$  and  $\Delta t$  of  $50 \text{ yr}$  gives the best convergence for the least computation, both from the Peclet and Courant numbers and from simple observation of the solution. The spatial location

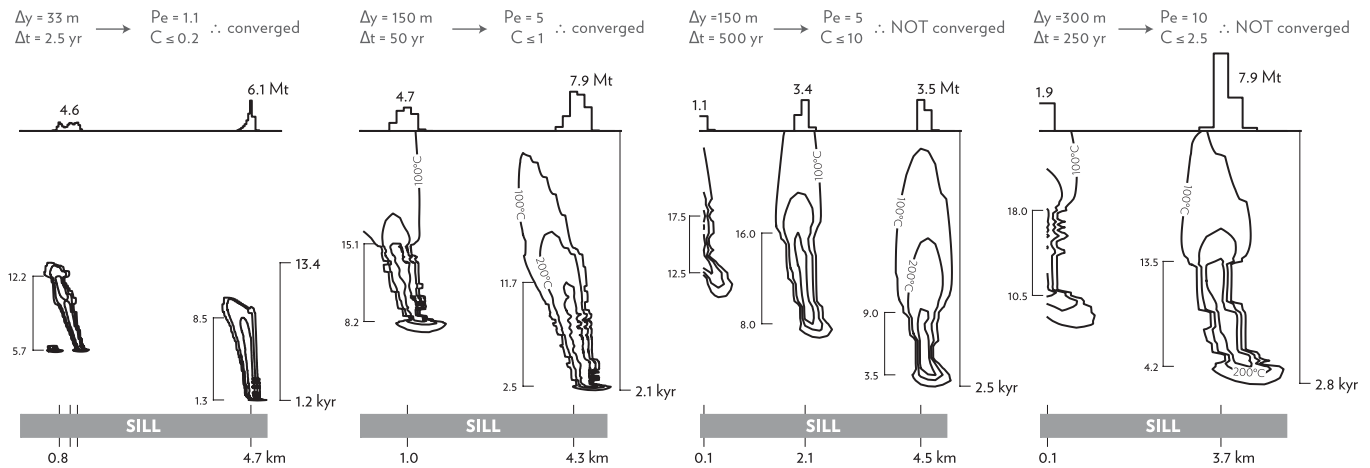


FIG. A1. Cumulative tons of zinc vented from each element across the top boundary (upper portions) and temperature of fluids venting as a function of time (lower portions) for cases with different grids ( $\Delta y$ ) and time steps ( $\Delta t$ ). The grid is refined relative to that shown in Figure 1 by increasing the number of elements in all quadrants by the same factor.

of the venting is not as well resolved and the venting continues longer at lower temperatures. However, the deposits are located in about the same positions on the sea floor and contain roughly the same tonnage of zinc metal and thus adequately characterize the aspects of the hydrothermal system we consider most important. This case took ~4 hours and is the refinement used in the other simulations throughout the paper.

The case with  $\Delta y$  of 300 m and  $\Delta t$  of 250 yr, on the other hand, is clearly not converged, either numerical or by observation. Of special note is the case with  $\Delta y$  of 150 m (adequate grid refinement) and  $\Delta t$  of 500 yr. The vents are well-formed

and the history of vent temperature is smooth. The calculation looks good, but the plumes develop as they do only because the thermal front moves across many grid cells in a single time step. The simulation is not converged, not valid, and very misleading.

